# DETERMINATION OF ICOSAHEDRAL VIRUS STRUCTURES BY ELECTRON CRYOMICROSCOPY AT SUBNANOMETER RESOLUTION

By Z. HONG ZHOU* AND WAH CHIU†

*Department of Pathology and Laboratory Medicine, University of Texas–Houston Medical School, Houston, Texas 77030, and †National Center for Macromolecular Imaging, Verna and Marrs McLean Department of Biochemistry and Molecular Biology, Baylor College of Medicine, Houston, Texas 77030



## I. Introduction

X-Ray crystallography is the method of choice for revealing atomic structures of large macromolecules and viruses. As shown in various examples in this volume, electron cryomicroscopy has emerged rapidly and has become a parallel technique to reveal additional information about virus structures, even in the situation in which the crystal structure of the virus may have already been obtained. The information that can be extracted from a hybrid approach of X-ray crystallography and electron cryomicroscopy is



*ADVANCES IN PROTEIN CHEMISTRY, Vol. 64*



0065-3233/03 $35.00

well illustrated in the article by Gilbert, Grimes, and Stuart (this volume). An exhaustive survey of electron cryomicroscopy applications related to viral assembly and virus cell entry has also been reviewed (Baker *et al.*, 1999).

In most of the applications of virus structure determination to date, electron cryomicroscopy has been used as a low-resolution technique (15–30 Å). Several studies have shown the feasibility of resolving the three-dimensional (3-D) structures of icosahedral virus particles at subnanometer (7- to 9-Å) resolution, where no crystal structures of the viruses or their components were previously known (Böttcher *et al.*, 1997a; Conway *et al.*, 1997; Trus *et al.*, 1997; Zhou *et al.*, 2000, 2001, 2003). Together with other biochemical and bioinformatics analyses, long helices inside the protein components of the viruses have been identified and their structural folds deduced. These developments represent a significant step forward because such *de novo* structure determinations have revealed new structural features and uncovered novel protein folds. Moreover, in the favorable event when a high-resolution model of individual protein(s) is available, the secondary structure elements identified inside the subunits of macromolecular assemblies by the electron cryomicroscopy approach provide internal markers to guide the fit of the atomic structures of the components when establishing a pseudo-atomic model of the entire assembly. These capabilities will make the hybrid approach more accurate, reliable, and powerful.

Because the methodology of obtaining subnanometer structures by electron cryomicroscopy is not yet a common practice, we focus in this article on reviewing this emerging technique, relating our own experiences and approaches. Readers interested in the general methods of virus reconstruction may refer to previous reviews on basic physical principles and procedures for low-resolution icosahedral particle reconstruction (Baker *et al.*, 1999; Thuman-Commike and Chiu, 2000) in addition to the original literature describing image-processing algorithms (Crowther, 1971; Conway and Steven, 1999; Zhou *et al.*, 1998; Fuller *et al.*, 1996; Baker and Cheng, 1996).

## II. Electron Cryomicroscopy

### A. *Theoretical Considerations of Electron Imaging*

A 3-D structure of an object viewed through an electron microscope is described in terms of the 3-D Coulomb potential function within the object. The image recorded in an electron microscope is a convolution of the projected potential function of the object with the contrast transfer

function (CTF) of the electron microscope (EM) (Erickson and Klug, 1970) and various other experimental factors (Jiang and Chiu, 2001). Because the electrons used here have wavelengths smaller than 0.2 Å, the depth of field [see Eq. (5) below] is large enough so that the top and bottom parts of the particle can be thought of as having the same focus. The deconvolution of the image can be conveniently carried out in Fourier space. In addition, the effect of the potential field of thin biological samples on the incident electrons is small (i.e., the so-called weak phase approximation), which allowed the relatively convenient formulation of the image formation theory (Erickson and Klug, 1970; Thon, 1971). Under this formulation, the Fourier intensity, $I(s)$, of an electron image as a function of spatial frequency, $s$, is expressed as (Ludtke *et al.*, 2001)

$$I(s) = F^2(s)\mathrm{CTF}^2(s)E^2(s) + N^2(s) \tag{1}$$

where

$$\mathrm{CTF}(s) = -k[\sqrt{1 - Q^2}\,\sin(\gamma) + Q\,\cos(\gamma)] \tag{2}$$

and

$$\gamma = -2\pi\left(\frac{C_s\lambda^3 s^4}{4} - \frac{\Delta Z\lambda s^2}{2}\right) \tag{3}$$

and $k$ is a scaling factor relating the arbitrary scale of structure factor, $\overline{F}\,(s,\theta)$, to the specific electron dose and film sensitivity. $C_s$ is the spherical aberration coefficient of the objective lens, $\lambda$ is the electron wavelength, and $\Delta Z$ is the objective lens defocus and is positive for underfocus in the convention used here. The image contrast contains two terms, one for phase contrast, $\sin(\gamma)$, and the other for amplitude contrast, $\cos(\gamma)$. $Q$ is the fractional amplitude contrast, and its value depends on the electron energy and specimen thickness. Under a given experimental setting, all the parameters in Eq. (3) are constant except $\Delta Z$, which is set by the microscope operator. Figure 1 shows the CTF curves in a 300-kV electron microscope for underfocus values of 0.5 $\mu$m (short-dashed curve) and 3.0 $\mu$m (long-dashed curve). At a low-resolution range, the values of CTF are smaller with a small defocus setting than those with a high defocus setting. Conversely, at a higher resolution range, there are fewer oscillations with a small defocus setting than with a high defocus setting. The modulation of Fourier amplitudes due to the CTF thus affects the contrast at various spatial frequencies, depending on the defocus setting of the micrograph.

According to Equation (3), when $\Delta Z$ is negative (overfocus) or has a small positive (underfocus) setting, $\gamma$ will have a negative value.

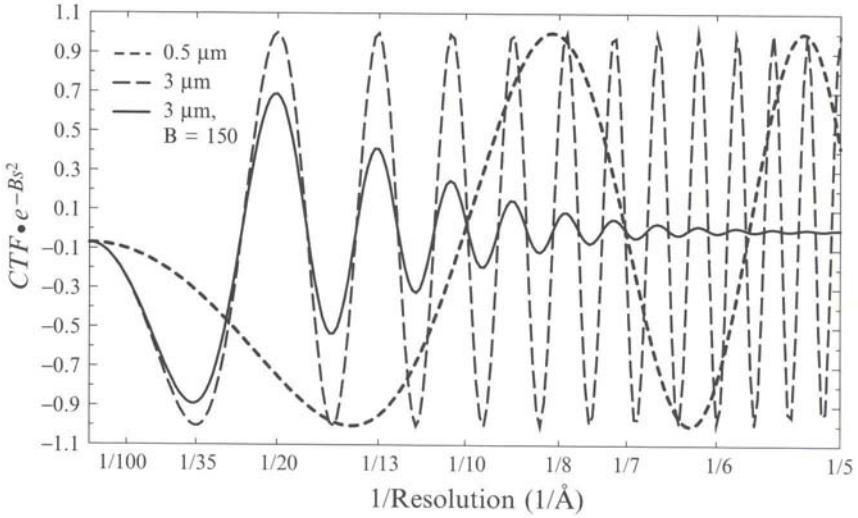


FIG. 1. CTF and $E$ function simulation. EM imaging parameters: electron energy = 300 keV; spherical aberration coefficient $C_s$ = 1.6 mm; $Q$ = 7%. No envelope decay ($B$ = 0) was used for the dotted (underfocus = 0.5 $\mu$m) and dashed (underfocus = 3.0 $\mu$m) curves.

Consequently the sine and cosine terms in Eq. (2) would have opposite signs at low frequency (i.e., small $s$), which leads to a poor low-resolution image contrast that is difficult to interpret for image processing. Therefore, micrographs are usually recorded with significantly underfocused settings (i.e., at least ~1–4 $\mu$m, depending on the voltage of the electrons used in imaging).

The cumulative envelope function, $E(s)$, can be complex and is attributable to a number of instrumental and experimental effects, such as spatial and temporal coherence and specimen motion. It has been shown that in practice a simple Gaussian function with width $B$ adequately describes the cumulative envelope function (Saad *et al.*, 2001):

$$E(s) = e^{-Bs^2} \tag{4}$$

Under this definition, the $E$ function is characterized by an experimental $B$ factor, which can be estimated experimentally (Saad *et al.*, 2001). Note that the cumulative $B$ factor applied in the final reconstruction is a composite of experimental and computational causes. The computational $B$ factor is attributable to additional blurring effects such as inaccuracy in determining the orientation of particles, which could also be described by a Gaussian function type. The dampening of the image contrast by the

function of a typical cumulative $B$ factor (150 $Å^2$) is steep at a resolution beyond 10 Å (Fig. 1, solid curve). Note that this dampening function is mathematically analogous to the crystallographic temperature factor. However, the physical causes of these dampening functions are different. Moreover, the $B$ factor as defined here is smaller by a factor of four than that used in the crystallographic formulation adopted in some studies (Böttcher *et al.*, 1997a).

### *B. Choice of Instrument*

Modern transmission electron cryomicroscopes are capable of routinely recording inorganic crystal lattice images beyond 2.5-Å resolution. Unfortunately, because of the constraint of radiation damage, it is not possible to use the same electron optical conditions to image ice-embedded virus particles. With the best imaging procedure, it is straighforward to obtain an image of ice-embedded virus particles with a detectable contrast signal of up to 7–9 Å. Indeed, some of the best resolution structures published so far were recorded with a 20-year-old instrument (Table I). The desirable specifications of an electron cryomicroscope for imaging virus particles in the 7- to 9-Å resolution range include a field emission gun, an electron voltage in the range of 200–400 kV, and a cryospecimen holder with a low-dose kit.

The primary reason for favoring the field emission gun is the high spatial coherence of its illuminating beam (Zhou and Chiu, 1993). The envelope function due to the partial spatial coherence of the electron beam is a function of defocus value and angular source size (Zhou and Chiu, 1993; Chiu, 1978). The field emission gun would allow the use of a smaller source size and large defocus value so that the low-resolution image contrast is high while the high-resolution contrast is still present. Without the field emission gun, it would be necessary to use a smaller defocus value to avoid the severe high resolution image contrast dampening due to the partial spatial coherence of electron source illumination (Zhou *et al.*, 2000, 2001). In this case, the low-resolution contrast would be rather low, making it difficult to recognize particle images. The use of a large defocus value at realistic angular source size can lead to dampening the image contrast at high resolution, as illustrated by the solid curve in Fig. 1.

There are several advantages of choosing higher voltages to record images. The first is the smaller chromatic aberration effect on the images; and the second is the larger depth of field [see Eq. (5) below]. As pointed out above, the formulation of the currently used virus reconstruction

TABLE I
Comparisons of Different Strategies Used in subnanometer Reconstructions

| Virus name, particle diameter | Voltage (kV) | Electron gun | Focal pair/ series | Range of underfocus ($\mu$m) | *B* factor[a] (Å$^2$) | Refinement method | No. of particles included in the final map | Effective resolution (Å) | Ref. |
|---|---|---|---|---|---|---|---|---|---|
| Herpesvirus capsid, 1250 Å | 400 | $LaB_6$ | Focal pair, discard far-from-focus images | 0.2–2.0 | 180 | 20 projections, common -line based | 5860 | 8.5 | Zhou *et al.*, 2000, 2001 |
| Cytoplasmic polyhedrosis virus, 850 Å[b] | 400 | $LaB_6$ | Focal pair, discard far-from-focus images | 0.3–2.8 | 180 | 20 projections, common-line based | 4532 | 8.0 | Liang *et al.*, 2002; Zhou *et al.*, 2003 |
| Rice dwarf virus, 780 Å | 400 | $LaB_6$ | Focal pair, discard far-from-focus images | 0.3–2.2 | 150 | 20 projections, common-line based | 3261 | 6.8 | Zhou *et al.*, 2001 |
| Semlike: Forest virus, 700 Å | 200 | FEG | Single focus | 0.98–7.6 | 15[c] | PFT | 5276 | 9[d] or 10.5 | Mancini *et al.*, 2000 |
| P22 phage, 680 Å | 400 | $LaB_6$ | Focal pair | 0.5–2.0 | 50–250 | 20 projections, common-line based | 8723 and 5000 | 8.5 and 9.5 | Jiang *et al.*, 2001a, 2003 |

| | | | | | | | | | |
|---|---|---|---|---|---|---|---|---|---|
| Papillomavirus capsid, 600 Å | 200 | FEG | Merged focal series | 1.4–2.7 | 0 | PFT | 209 | 9[d] | Trus *et al.*, 1997 |
| Hepatitis B virus core, 360 Å | 120 | FEG | Merged focal pair | 0.86 and 2.2 | ~100[c] | PFT | 600 particle pairs | 9[d] | Conway *et al.*, 1997 |
| Hepatitis B virus core, 360 Å | 200 | FEG | Single focus | 1.3–1.5 | 125 | 6 projections, common-line based | 6384 | 7.4 | Böttcher *et al.*, 1997a |
| Tomato bushy stunt virus, 300 Å | 200 | FEG | Sinogram | Unknown | Unknown | Projection matching between class averages and projections | ~6000 | 5.9[d] | van Heel *et al.*, 2000 |

*Abbreviation:* PFT, Polar fourier transform; FEG, Field emission gun.

[a]There is a factor-of-four difference between the definitions of the *B* factor used by the MRC group (Böttcher *et al.*, 1997a) and those used by others (Conway *et al.*, 1997; Zhou *et al.*, 2000, 2001, 2003). The *B* factors shown have been adjusted to follow the definition of Eq. (4) described in text.

[b]Diameter measured including the poorly ordered A spike. When excluding the A spike, cytoplasmic polyhedrosis virus has a diameter of 710 Å.

[c]The low-resolution features have also been additionally down-weighted in these studies.

[d]Resolution assessment based on the $3\sigma$ or other criteria that are less stringent than the 0.5 FSC or 45° phase difference criteria.

methods are all based on the assumption that the top and bottom parts of the particle have equivalent focus. However, as can be derived from Eq. (3), the difference in the defocus-related phase modifications between the top and bottom surfaces of a specimen with a thickness $t$ is

$$\Delta\gamma = \pi \cdot t \cdot \lambda \cdot s^2 \tag{5}$$

Thus, if $\pi/2$ is allowed to be the maximum tolerable phase error, there is a constraint on the maximum thickness [commonly referred to as the depth of field, that is, $t = 1/(2\lambda \cdot s^2)$] for a given accelerating voltage and at a given target resolution. For instance, the maximum thickness of a particle for a 7-Å resolution structure must be less than 1500 Å with a 400-kV instrument. Figure 2 gives the maximum thickness of a particle for 100–400 kV as a function of spatial frequency. Therefore, there is a compelling reason to use as high a voltage as possible if high-resolution studies with large virus particles are to be pursued.

The cryoholder is used to keep the specimen in a frozen hydrated state in addition to reducing radiation damage. Several types of cryoholders operated at either liquid nitrogen or liquid helium temperature are now

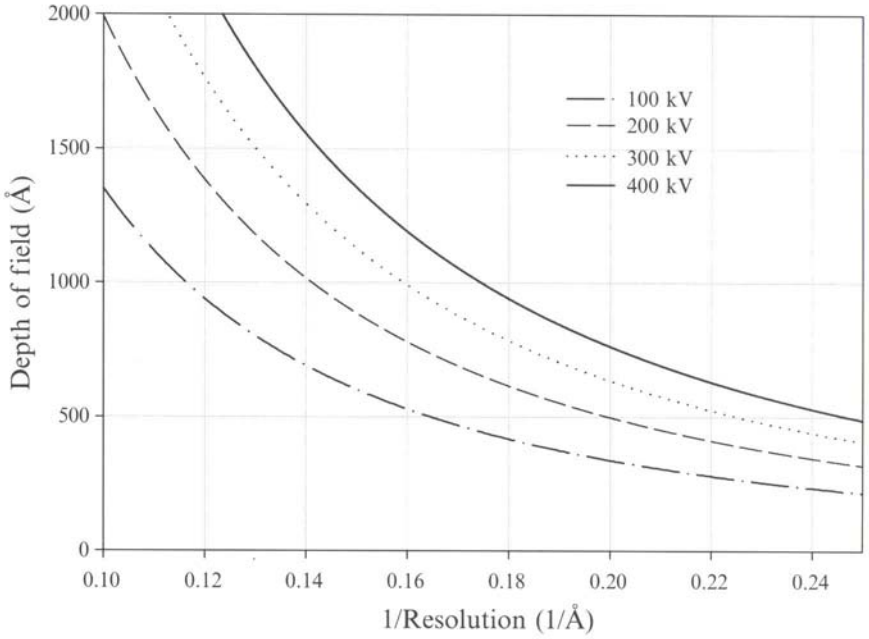


FIG. 2. Depth of fields at 100, 200, 300, and 400 kV as a function of reciprocal resolution.

available and are sufficiently stable for recording data between 7 and 9 Å from ice-embedded virus particles. The low-dose option is now available in all electron cryomicroscopes. Their modes of operation vary depending on the instruments but are generally operationally effective. For subnanometer resolution, the cumulative electron dose should be less than 15 electrons/Å$^2$ at liquid nitrogen specimen temperature (Schmid *et al.*, 1993). The reduction in radiation damage at liquid helium temperature is no more than a factor of 1.5 to 2, relative to the liquid nitrogen temperature (Chiu *et al.*, 1981). Therefore, it is essential to closely monitor the data collection procedure to avoid overdosing the specimen. Images suffering from radiation damage appear fuzzy or lack detailed features even though their incoherently averaged Fourier transforms may reveal excellent CTF rings. In more severely overdosed micrographs, bubbles can be seen around particle images.

### C. *Number of Particle Images Needed for a Three-Dimensional Reconstruction*

On the basis of geometric consideration alone, the number $N$ of particle images of different views needed for reconstructing a 3-D structure of a large asymmetric complex is dependent on targeted resolution $d$ and particle diameter or specimen thickness $t$, that is, $N = \pi t/d$ (Crowther *et al.*, 1970a). Because of the redundancy of 60 copies of asymmetric units in an icosahedron, $N$ is reduced 60-fold. For example, a 1250-Å-diameter icosahedral particle requires as few as 17 evenly spaced views to compute a 4-Å map. However, the signal/noise ($S/N$) ratio is low in low-dose images, particularly those recorded at close-to-focus conditions. The number of views required for a 3-D reconstruction is thus dependent not on particle size, but on the targeted resolution and many other experimental factors, including the $S/N$ ratio in the low-dose image, the structural integrity of the particles and the computational accuracy of the particle orientation parameters determined. In practice, 4000–10,000 particles have been used to reconstruct a 7- to 9-Å map (see Table I).

## III. Overview of Methods for Subnanometer-Resolution Reconstructions

Several structures of icosahedral particles with diameters in the range of 300–1250 Å have been reported to reach a subnanometer resolution to date. Different methods of data collection and analyses were used. Table I summarizes the characteristics of the data acquisition and data processing

in the order of the structural complexity or particle diameters. All these studies were carried out with 120- to 400-kV electron cryomicroscopes with liquid nitrogen specimen cryoholders. Most were equipped with a field emission gun to obtain the maximum spatial coherence of the illuminating electrons. The methods differ primarily in the corrections of the CTF and cumulative *B* factor and in the methods of refining the orientation and center parameters of particle images.

### *A. CTF and B Factor Corrections*

The defocus values for electron micrographs can be readily estimated on the basis of the CTF rings visible in the incoherently averaged Fourier transforms of individual particle images (Zhou *et al.*, 1994, 1996). This method has become a routine practice universally adapted for the initial evaluation and determination of CTF parameters as defined in Eqs. (2) and (3). So far, the determination of the cumulative *B* factors for 3-D reconstruction has been somewhat *ad hoc*. The cumulative *B* factor used in these studies is determined either by trial and error with the initial value derived from previous results, or from the incoherently averaged Fourier transforms of particle images. Different approaches have been adopted to make corrections for the CTF and the *E* function of the micrographs. They differ in the steps where these corrections are made and in whether or how the *E* function is corrected.

Zhou and Chiu made the CTF and *B* factor corrections at the image level and the details of corrections differed at different stages of data processing. The defocus and other parameters were estimated by fitting of the functions with the profile of incoherently averaged Fourier intensities of particle images (Zhou *et al.*, 1994, 1996; Ludtke *et al.*, 1999). In some of their studies, they utilized the X-ray solution scattering intensity of the viral particles to provide a one-dimensional profile of the structure factor of the virus particle (Fig. 3) for the estimation of the *B* factors of the micrographs (Saad *et al.*, 2001). Immediately before the merging of Fourier data of all the particles, the Fourier amplitude of each particle image was corrected by dividing the CTF and the Gaussian function, using a modified Wiener type of filter function by which the data points near the CTF zeros were excluded to avoid amplifying the noise in these regions (Zhou *et al.*, 1994, 1999, 2000, 2001). However, in the initial and other intermediate reconstructions generated during the orientation and center refinement, only CTF correction without the *B* factor correction was performed. For orientation and center refinement, particles from each micrograph were refined by minimizing their difference with model

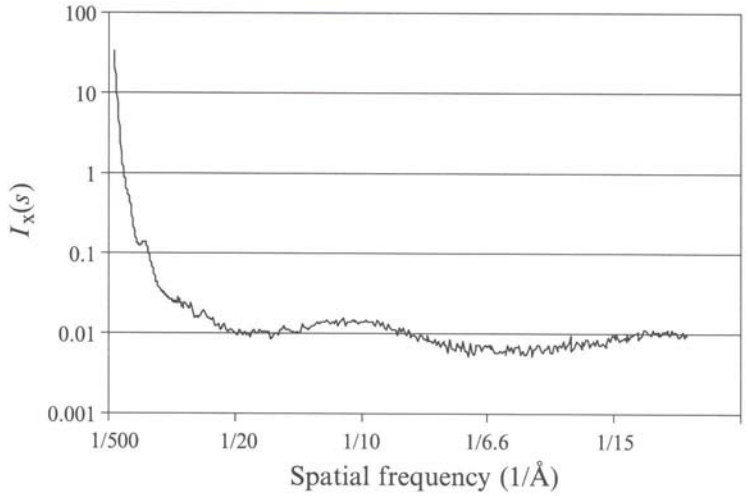


FIG. 3. X-ray solution scattering intensity of a suspension of herpes simplex virus 1 B capsids recorded at the Stanford SLAC beam line. [Adapted from Saad *et al.* (2001) with permission from the publisher and the author.]

projections, which were multiplied by a CTF function determined for the micrograph. The final reconstruction was synthesized from the Fourier data of particle images corrected by CTF and $B$ factor.

A slightly different approach of CTF and $E$ function correction was used by Conway, Trus, and Steven (Conway *et al.*, 1997; Trus *et al.*, 1997; Conway and Steven, 1999). For each micrograph an $E$ function was empirically determined by fitting to a Gaussian curve with four parameters. The CTF, also determined from incoherently averaged particle images, and the $E$ functions were then corrected in the particle averages generated by combining the Fourier transforms of micrographs in a focal pair/series, using a formulation with a Wiener-like filter (Conway *et al.*, 1997; Trus *et al.*, 1997; Conway and Steven, 1999). Three-dimensional maps were subsequently generated from these CTF-corrected particle averages. In their approach, the low-resolution terms (within the first peak of CTF) were left uncorrected, presumably to down-weight the low-resolution feature in the 3-D reconstruction.

van Heel and colleagues favored performing the CTF correction directly on the micrographs at the beginning of data processing (van Heel *et al.*, 2000). In addition, the CTF correction was performed separately in different areas of each micrograph because of defocus variation across the micrograph in their data (van Heel *et al.*, 2000). In their case, phase

reversal was corrected without amplitude scaling to avoid amplifying the noise present in the image.

Böttcher and Crowther made the CTF correction at the 3-D map level (Böttcher and Crowther, 1996; Böttcher *et al.*, 1997b). They first determined a medium-resolution 3-D map from the particles in a single micrograph. The CTF parameter of the micrograph was determined by cross-correlating its CTF-uncorrected 3-D reconstruction with a CTF-corrected model. The correlation coefficient as a function of spatial frequency has the same positive and negative oscillation patterns as the CTF of the micrograph. Thus the positions of CTF zeros can be identified by finding the locations where the correlation coefficient reaches zero. Many of these CTF-uncorrected maps with the determined CTF parameters were then merged to generate a CTF-corrected map by least-squares fitting. The map was further scaled with a Gaussian function with a cumulative *B* factor based on other studies (Böttcher *et al.*, 1997a,b). The rationale for using this approach was that relatively noise-free uncorrected 3-D maps could be used to determine the CTF parameters more accurately. However, this approach is impractical for large viruses, for which an insufficient number of particles can be obtained on a single micrograph at an appropriate magnification to generate a CTF-uncorrected map with subnanometer resolution data.

The defocus accuracy achieved on the basis of the incoherent averaging of particle Fourier transforms (Zhou *et al.*, 1996) may not be sufficient to correct the CTF for micrographs with relatively large defocus values because of the close proximity of CTF oscillations in the high spatial frequency region. For such micrographs, it is desirable to refine the estimated defocus values by taking advantage of an existing model (Böttcher *et al.*, 1997a). For larger virus particles, for which it is impractical to obtain a 3-D reconstruction from a single micrograph, we would calculate the average Fourier ring correlation (FRC) function between a particle image of unknown defocus with its corresponding projections computed from the latest CTF-corrected model. The average of the FRC functions of all particles in the same micrograph should yield a relative noise-free curve to locate the CTF zeros. The experimental *B* factor of each micrograph can also be determined. Initially, it may simply be assumed that the structural factor profile in the subnanometer region is a flat curve to obtain a rough *B* factor estimate for each micrograph by fitting to the profile of the incoherently averaged Fourier transforms of particle images. A more plausible approach is to use generic models such as atomic models of related protein complexes or of particles of similar dimension and shape to approximate the structural factor profile of the particle for *B* factor estimation.

### B. *Orientation and Center Determination*

van Heel and co-workers used a real space common-lines (i.e., sinograms) algorithm to determine and refine the center and orientation of particle images, as applied to asymmetric particle reconstruction (van Heel *et al.*, 2000). In other laboratories, two completely different methods of orientation estimation and refinement have been employed: the Fourier common-lines method (Crowther *et al.*, 1970b) and the polar Fourier transform (PFT) method (Baker and Cheng, 1996). The Fourier common-lines method can be used without an initial model and has often been employed at the beginning of a project. After an initial model becomes available, either of these methods can be used to carry out particle parameter refinement iteratively by minimizing the differences between the raw particle image and a set of computed projections of the latest reconstruction. The parameters of minimization are different in the two methods. The Fourier common-lines method is based on the phase residual differences, whereas the PFT method is based on the correlation matching. The PFT method (Baker and Cheng, 1996) has the flexibility to circularly mask either the inner or outer components in real space and has been used in structural determination up to 9 Å (Conway *et al.*, 1997; Trus *et al.*, 1997; Mancini *et al.*, 2000). On the other hand, the Fourier common-lines method is capable of refining the positional parameters and Euler angles simultaneously (Zhou *et al.*, 1998) and has been successfully used to reach 6- to 7-Å resolutions (Böttcher *et al.*, 1997a; Zhou *et al.*, 2001).

## IV. Example of Data Collection, Evaluation, and Processing

Using the procedure illustrated in Fig. 4, we have determined several subnanometer-resolution structures of icosahedral particles (Zhou *et al.*, 2000, 2001, 2003; Viang *et al.*, 2001a, 2003; Liang *et al.*, 2002). In this section, we discuss each of the steps in our procedure and mention the specific modular programs (in *italics*) employed.

### A. *Imaging*

Most of the subnanometer-resolution studies used field emission gun cryomicroscopes because of the advantages mentioned above (Table I). When the $LaB_6$ gun is used, the spatial coherence of the instrument is relatively poor. Therefore, a high-resolution image must be recorded with a small defocus value to minimize the dampening due to the partial coherence envelope function (Zhou and Chiu, 1993). Consequently, these images have low contrasts for their low-resolution features, making it difficult to locate the particles and to determine their initial orientation

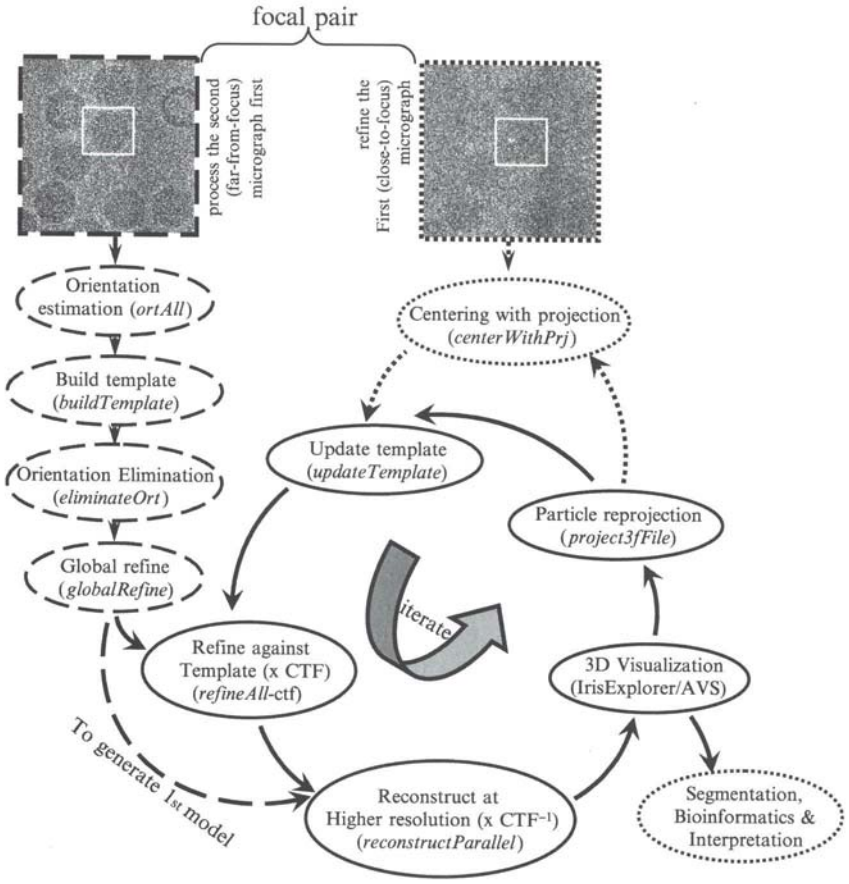


FIG. 4. Flow chart of data processing, using the focal pair approach (Zhou *et al.*, 1995, 1998; Liang *et al.*, 2002). In this approach, the far-from-focus micrograph (*top left*) is used to assist in orientation determination of particles in the close-to-focus micrograph (*top right*). Data-processing steps are listed, inside dashed-line ovals (for far-from-focus particles), dotted-line ovals (for close-to-focus particles), or solid-line ovals (for both far-from-focus and close-to-focus particles). The procedure begins with far-from-focus particles, first by obtaining a set of possible orientation estimates for each particle, using self common-line phase residual minimization, establishment of a template set of particles, followed by the elimination of incorrect orientation estimates, and then global simultaneous orientation and center refinement, using particle images (Zhou *et al.*, 1998), and finally 3-D Fourier merging and inversion by Fourier–Bessel synthesis. The 3-D merging and orientation refinement steps are iterated for several cycles, each time with the update of the template set through the computation of 2-D projections from the latest 3-D reconstructions. The center of each close-to-focus particle image is first determined by cross-correlating the particle image with a computed projection along the orientation estimated from the corresponding far-from-focus particle (*Centering with Projection*). The orientation and center parameters are

parameters confidently. An experimental solution is to use the so-called focal pair method [Figs. 4 and 5a–d; see detailed description elsewhere (Liang *et al.*, 2002)]. In this method, the first micrograph is taken with a small defocus value (typically with an underfocus value such that the first CTF zero occurs at about 10 Å) to maximize the high-resolution signals and to increase the separation of neighboring CTF rings in the subnanometer spatial frequency range. The second, far-from-focus, micrograph is taken from the same specimen area at relatively higher defocus value (typically targeting the first CTF zero at about 20–30 Å, depending on the morphology of the particles imaged) to maximize the image contrast in the low spatial frequency range. The high contrast of low-resolution features of the far-from-focus micrograph is essential for the initial estimation of particle position and orientation. The particle orientation parameters estimated from this micrograph are then used as the starting point to refine those for the corresponding particles in the first, close-to-focus micrograph. In the final reconstruction, only the particles from the close-to-focus micrographs are included.

Although the use of the focal pair method doubles the task of image acquisition and their subsequent processing, it offers the most reliable means to eliminate false orientation assignments, which often occur for close-to-focus particle images. It should be pointed out that the focal pair approach was not used with the structures determined with microscopes equipped with a field emission gun, by which the micrographs were recorded with relatively large underfocus values. However, when extending structural analysis beyond 7–9 Å, the focal pair approach may be necessary even with the use of a field emission gun. This is because adjacent CTF rings present in the micrographs with large defocus values may be too close to one another in the high spatial frequency range to achieve accurate CTF determination and correction.

### *B. Digitization and Particle Selection*

Before digitization, micrographs are first examined visually to discard those with apparent image astigmatism or drift. So far, all the image data used in subnanometer-resolution reconstructions have been recorded on

---

refined iteratively toward higher resolution against a template set of a list of CTF-multiplied, evenly spaced projections made from the current best model. Usually about 20 projections are used so that the Fourier transforms are fully sampled. In each iteration, the resolution of the reconstruction is gradually improved by including image data at a higher spatial frequency range. Note that the final 3-D reconstruction includes only particle images from the close-to-focus micrographs.

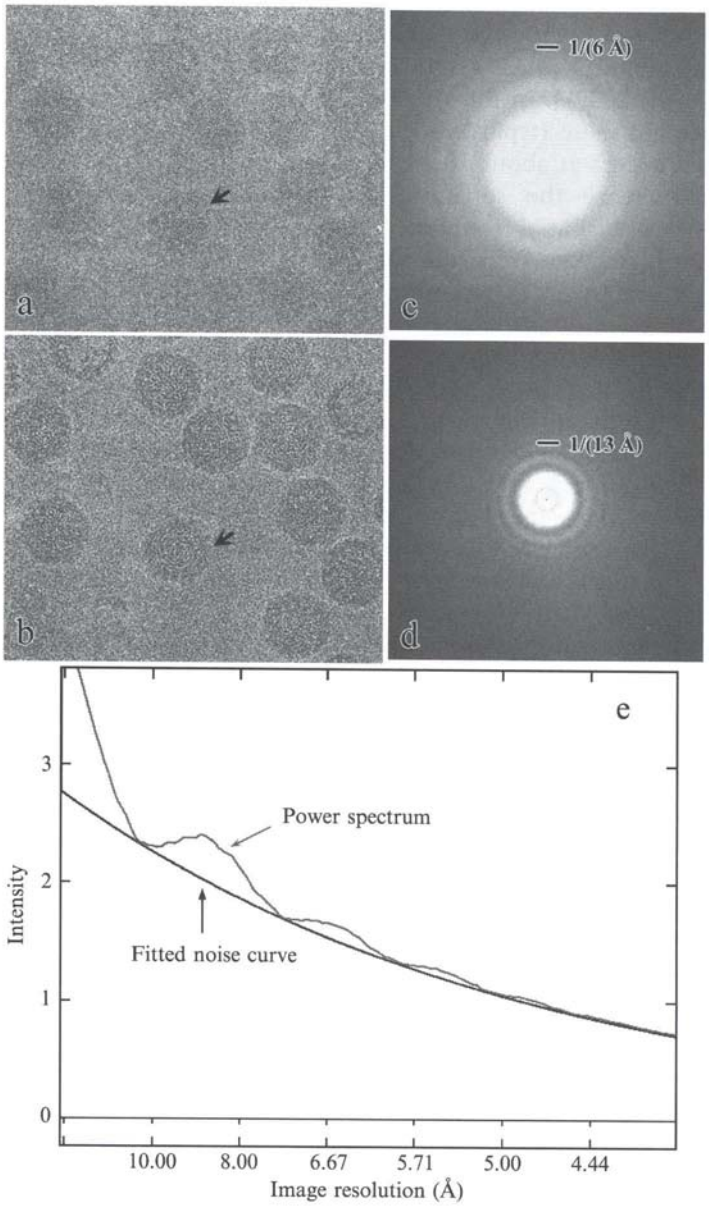


FIG. 5. Imaging and image quality assessment by incoherent averaging of Fourier transforms. (a and b) A focal pair of 400-keV electron micrographs of ice-embedded rice dwarf virus (RDV) was recorded in a JEOL4000 electron cryomicroscope with a Gatan cryoholder operated at $-170^{\circ}$C. Images were taken at $\times$50,000 magnification with an electron dose less than 20 electrons/Å$^2$. One corresponding RDV particle is

photographic films and, consequently, must be digitized in a high-resolution film scanner with minimal modulation transfer function. The digitization step on the specimen scale should be approximately three to four times finer than the expected resolution of the 3-D reconstruction. The step size limits of 7.5–10 $\mu$m/pixel of currently available high-speed film scanners thus require that the micrographs be taken at relatively high magnification (×50,000–60,000). At such a magnification, the specimen exposure dose limit of 10–15 electrons/Å$^2$ is sufficient to produce an acceptable optical density on the photographic film.

The digitized micrographs are subject to further graphical inspection for particle selection. This step is typically performed on a graphics workstation with a large memory because each micrograph is rather large (~0.5 GB for each micrograph scanned at 1.4 Å/pixel on the specimen scale). In practice, particles are picked either manually or semiautomatically and saved to image particle files, using graphic tools such as *boxMrc* (Liang *et al.*, 2002) and *EMAN* (Ludtke *et al.*, 1999). These tools are also able to automatically match corresponding particles on focal pair micrographs.

### C. *Image Screening*

Before embarking on extensive data processing, a number of screening steps are routinely performed to select particles appropriate for subnanometer-resolution reconstructions. Examining the power spectrum or incoherently averaged Fourier transforms of particle images is the first step to assess the quality of images as shown in Fig. 5c and d (Zhou *et al.*, 1994, 1996; Ludtke *et al.*, 1999). The most frequently encountered image defects are subtle beam-induced movement (such as charging) and specimen/cryostage drifting, which manifest as nonisotopic or incomplete CTF rings in the power spectrum of particle images (Thuman-Commike and Chiu, 2000). In some micrographs, specimen charging is localized to a small region, resulting in different power spectra for particle images at different locations on the same micrograph.

A potentially difficult problem is ice thickness variations across a micrograph, which would result in defocus difference at different regions

highlighted by arrows. (c and d) Incoherently averaged Fourier transforms of individual RDV particle images selected from micrographs shown in (a) and (b), respectively. Each spectrum was obtained by incoherently averaging the Fourier transforms of about 100 particle images. (e) Circularly averaged Fourier intensity as a function of resolution from the power spectrum in (c). The profile indicates that the close-to-focus micrograph has detectable contrast beyond 5-Å resolution.

on the same micrograph. Changes in ice thickness are evident from variations in the particle contrast. These variations can affect the accuracy in determinating the effective CTF of the micrograph and further complicate the problems imposed by the depth of field limit for large particles (Fig. 2).

### *D. Orientation and Center Determination by the Focal Pair Method*

As mentioned above, we used the focal pair method in the orientation and center determination for subnanometer-resolution structure determination. In this method, the orientation parameters obtained from the far-from-focus particle images are used as the starting point for processing the corresponding close-to-focus particles in a focal pair. The center parameters of each of the close-to-focus images are determined by focal-pair matching during particle selection and refined by cross-correlation with computed projections of a preliminary 3-D model calculated from the far-from-focus micrograph. These center and orientation parameters are further refined gradually, using template-based refinement by including image data at higher spatial frequency range until the resolution of the map can no longer be improved. Only the close-to-focus images are included to compute the final high-resolution reconstruction. Some of these key steps are described in more detail below.

#### *1. Initial Estimation of Orientation and Center Parameters*

The first task is orientation and center estimation, or orientation search (*ortAll*), for all particles selected from far-from-focus micrographs. In this program, each of the selected particles is first premasked with a Gaussian mask to exclude noise from the corners and to reduce Fourier artifacts (Frank, 1979). The size of the mask is typically slightly larger than the particle diameter. Artifacts that occur when no mask is used typically manifest as a cross at the origin of the Fourier transform, due to the noncontinuity in densities at opposing edges of the particle. The particle center, defined as the projection of the origin of the icosahedral axes in the image plane, is approximated by locating the peak in the correlation image between the premasked particle and a reference image. The reference image can simply be the particle image itself rotated by 180°, or a rotationally averaged image sum of many particle images or computed projections generated by *azimuthalAvg*. The estimated center of each particle is used to remask the particle.

For each masked particle, a list (~30) of the most likely angular and center parameter estimates is obtained by sorting all possible orientations

according to their corresponding self common-line phase residuals calculated in a brute force manner at 1° intervals for the three angular parameters ($\theta$, $\phi$, and $\omega$) over the entire icosahedral asymmetric unit (Crowther, 1971). Four slightly different self common-line based formulations are evaluated in this brute force calculation (Crowther, 1971; Prasad *et al.*, 1988; Fuller, 1987; Baker *et al.*, 1988), only using particle Fourier data within the spatial frequency range of 1/35–1/300 $\text{Å}^{-1}$. Except for the Crowther formulation, these functions employ statistical measures such as the Student $t$ test (Prasad *et al.*, 1988) and the $\chi^2$ distribution (Fuller, 1987) to reduce estimation errors resulting from self common-line degeneracies. Self common-line degeneracy arises when the direction of view coincides with any of the 5-, 2-, and 3-fold symmetry axes, leading to fewer than 37 pairs of self common-lines in the Fourier transform of a particle image and smaller phase residuals if not down-weighted properly (Crowther, 1971).

### 2. *Orientation Elimination and Selection*

The Orientation Elimination program (*eliminateOrt*) sorts the lists of possible orientation and center estimates according to the cross common-lines phase residuals between the particle and a template set of particles or computed projections. The template set can be obtained by *buildTemplate* (when no preexisting model available) or *project3fFile* (when a preliminary model available) and consists of a group of either particle images with refined orientation and center parameters or projections computed from the best reconstruction available. During the execution of the *eliminateOrt* program, two cycles of coarse refinements are first performed, typically using particle Fourier data in the spatial frequency range of 1/300–1/30 $\text{Å}^{-1}$, for each listed set of center and orientation parameters before their ranking of cross common-lines phase residuals. For each particle, if the set of orientation and center parameters with the smallest cross common-line phase residual is smaller than a user-supplied cutoff, the particle with this set of orientation and center parameters is kept, or otherwise is "eliminated," for further processing. The phase residual cutoff is typically about 45–55°, depending on the low-resolution contrast (a function of defocus) of the particle images. The use of cross common-lines and a template set with more than one particle projection in *eliminateOrt* effectively eliminates the "inaccuracy near symmetry axes" problem associated with self common-line degeneracy that is often encountered in self common-lines based procedures (such as *ortAll*). The result of the *eliminateOrt* procedure is a subset of particles selected for further refinement.

*3. Orientation and Center Refinement*

Orientation and center parameters are refined by minimizing the cross common-line phase residuals between each particle and all other particles (*globalRefine*), and/or between the particle and a set (~20) of model projections (*refineAll*). These two approaches are known as Global Refine and Refine against Template, respectively. Both procedures carry out simultaneous orientation and center refinement, using Fourier common-lines. The computation time of *refineAll* is linear with the number of particles (~10 s/particle in a PC with a single 2-GHz Intel Pentium IV CPU). On the other hand, the computation time of the global refinement procedure increases quadratically with the number of particles and thus can be prohibitive for refining a large set of particles (Zhou *et al.*, 1998). However, global refinement does provide a useful alternative in two situations: the first being the initial stage of reconstruction when a template or a model is not yet available; the second being the refinement of close-to-focus images in the same defocus group, such as particles from the same micrograph.

In practice, the major portion of refinement is carried out by the iterative template-based refinement procedure (*refineAll*), which uses the CTF-corrected 3-D map as a template to refine all particles in the entire data set. The projections from a CTF-corrected model are first multiplied by the CTF of the particle image before refinement. This approach avoids the CTF correction on the particle images, thus avoiding possible noise amplification due to division by zero or by small CTF values near CTF zeros. Note that additional particles with incorrect parameters may be eliminated in this step because data at higher resolution are included in the refinement to provide more discriminating power. Once an adequate number of particles is accumulated on the refined list of orientation and center parameters, these particles are merged to calculate a new reconstruction, which can then be used to generate the current template set (*project3fFile* and *updateTemplate*). Typically it is necessary to iterate the above-described steps of orientation and center estimation, elimination, and refinement for three to five cycles until no more particles can be added to the list of refined particles.

*4. Center and Orientation Refinement for Close-to-Focus Images*

The orientation parameters obtained from the far-from-focus particle images in the focal pair are used as the starting point for processing the close-to-focus particles. Because of the poor $S/N$ ratio of low-resolution features, the center and orientation parameters of the close-to-focus particles cannot be reliably determined by directly using the orientation

estimation and selection steps described above. Typically, the center of each close-to-focus particle image in the entire data set is determined by focal pair matching and refined by locating the peak in the cross-correlation image (*centerWithPrj*) of the particle image and a projection computed in the same orientation as determined from its corresponding far-from-focus particles (*project3fFile*). Further refinement of the center and orientation parameters of all these particles is carried out by gradually (at an increment of 1–3 Å each iteration) extending toward the targeted resolution, using *refineAll* (or *globalRefine*) and 3-D reconstruction (see Section IV.E, below) programs.

### *E. Three-Dimensional Reconstruction by Fourier–Bessel Synthesis*

The last major tasks of data processing are data merging and reconstruction by 3-D Fourier inversion, using the Reconstruct program (Fig. 4, *reconstructParallel*). Instead of performing a direct 3-D inverse Fourier transformation, Fourier–Bessel synthesis is used to avoid an explicit interpolation in the 3-D Fourier space, thus allowing irregularly spaced Fourier transforms to be conveniently merged and averaged for 3-D Fourier inversion (Crowther, 1971). The program for the Fourier–Bessel synthesis as incorporated in our package was recoded on the basis of various previous implementations (Crowther, 1971; Prasad *et al.*, 1988; Baker *et al.*, 1988) to improve accuracy and to allow a much more efficient merging of large numbers of particles for higher resolution reconstruction. This program consists of four major computational steps. The first step prepares the normal matrices by applying one 5-fold, one 3-fold, and two 2-fold symmetry rotations to the Fourier transform of each particle to generate 60 Fourier "planes" in 3-D Fourier space for each particle. Before merging the Fourier planes of all the particles, the Fourier values (both phases and amplitudes) are corrected for CTF (Section III.A) (Zhou *et al.*, 1999). The Fourier values near the CTF zeros (e.g., $|CTF| < 0.15$) are simply discarded, thus avoiding potential problems of noise amplification. One normal matrix is prepared for each annulus in the polar coordinates of the 3-D Fourier space. The normal matrices are then solved by a linear algebra method for the discrete Fourier–Bessel transform values. This is followed by the summation of Bessel functions of different orders and the final step of Fourier–Bessel synthesis to compute a 3-D density map.

The computation time for the 3-D reconstruction depends mainly on the normal matrix preparation step and the Fourier–Bessel synthesis step. The time for the normal matrix calculation increases roughly linearly with the particle numbers and the targeted resolution. The Fourier–Bessel

synthesis step is independent of the number of particles but its computation time increases roughly cubically with the targeted resolution. Thus, although the execution time of this procedure could be rather lengthy [e.g., it took a full day on a 24-processor SGI Origin to calculate an 8.5-Å herpesvirus capsid map (5)], it is substantially faster than other real space reconstruction methods (e.g., the back projection reconstruction), whose computation time increases cubically with the targeted resolution and linearly with the number of particles. In addition, we have ported our Fourier–Bessel reconstruction program to run as parallel processes on both the SGI Iris shared memory platform and the Linux cluster distributed memory platform.

### *F. Assessment of Effective Resolution*

The quality of 3-D reconstructions should be assessed at various steps of the data processing to ensure data convergence and to measure the effective resolution of the final 3-D map. An obvious measurement that should be performed is to calculate the cross-correlation coefficient of the computed 3-D reconstruction and the true structure of the object. However, because the true structure is the very entity that is being reconstructed and, thus, is unknown in most situations, it is impossible to perform such a comparison. Instead, a widely used approach is to estimate how well two independent reconstructions agree with one another by calculating the differential phase residues (DPR) (Fig. 6a) and the Fourier shell correlation (FSC) coefficients (Fig. 6b) between the two maps (Böttcher *et al.*, 1997a; Zhou *et al.*, 1994; van Heel, 1987). The spatial frequency, where the FSC reaches 0.5 or the DPR increases to 45°, is commonly considered to be the effective resolution of the reconstructions; therefore, the term "resolution" does not really mean resolvability so much as reproducibility.

To monitor the progress of the reconstruction, the resolution test would be performed as a function of particle numbers. As shown in Fig. 6, the resolution would be expected to improve as the number of particles increases. Thus such a plot could allow the prediction of the number of particles needed to achieve a certain resolution. The required number of particles varied somewhat in practice (Table I), probably because of variations in the robustness of icosahedral symmetry in the particle, the image quality, as well as the effectiveness of the data processing procedures used. It should be pointed out that the FSC should approach unity at low resolution and generally decrease rapidly closer to the resolution limit for perfectly icosahedrally ordered particles. The presence

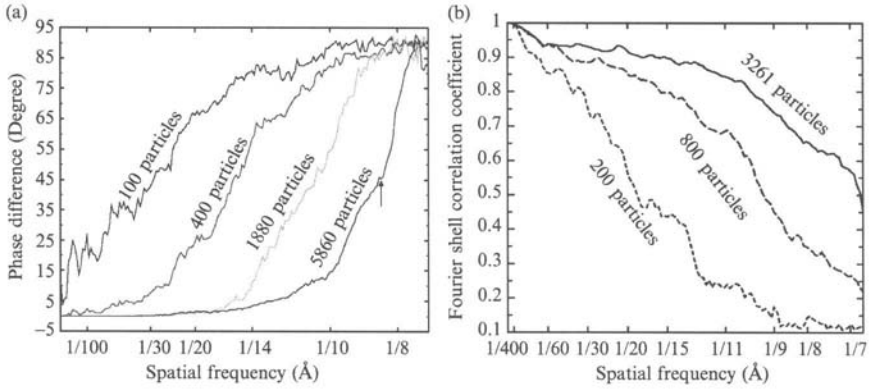


FIG. 6. Resolution assessments. (a) Differential phase residual method based on the 45° phase difference criterion used in the 8.5-Å resolution (indicated by arrow) structure of the herpesvirus capsid (Zhou *et al.*, 2000). (b) Fourier shell correlation method based on the 0.5 Fourier shell correlation coefficient criterion used in the assessment of effective resolution of the rice dwarf virus (RDV) structure at 6.8 Å (Zhou *et al.*, 2001). The imperfect FSC value (<1.0) is partly due to the presence of nonicosahedrally ordered dsRNA genomes within the RDV virions. [Adapted from Zhou *et al.* (2000, 2001), with permissions from the publishers.]

of nonicosahedrally ordered materials such as nucleic acid may lead to a less than unity FSC at low resolution.

### *G. Practical Use of Software Packages*

The data set for structure determination of an icosahedral particle of a moderate size (300–1200 Å in diameter) at subnanometer resolution typically needs 30–200 focal pairs of micrographs containing several thousands of particle images (Table I). For example, the number of particles increased about 40 times, from 159 to 5900, to improve the herpesvirus capsid reconstruction from 25 Å (Zhou *et al.*, 1994) to 8.5 Å (Zhou *et al.*, 2000). Table II shows the size of the data sets for various particle diameters for four targeted resolutions. Notably, the amount of data involved for a near atomic resolution reconstruction of a 1200-Å particle is nearly 1 terabytes (TB) and is almost 1 million times more than that needed for a low-resolution small particle reconstruction.

To engage in the investigation of structures at subnanometer resolution, inexperienced users often encounter two challenges: the first is to manage the large number of particle images efficiently and the second is to carry

TABLE II
Estimated Data Size, in Gigabytes, for Icosahedral Reconstruction of Different Particle Diameters at Different Resolutions[a]

| Diameter | Resolution (Å) | | | |
|---|---|---|---|---|
| (Å) | 24 | 12 | 8 | 4[b] |
| 300 | 0.008 | 0.21 | 2.8 | 54.4 |
| 700 | 0.048 | 0.96 | 12.6 | 248 |
| 1200 | 0.13 | 2.8 | 34.1 | 671 |
| 2000 | 0.41 | 7.7 | 89.4 | 1773 |

[a]Image data are stored as floating point numbers. A working disk space consumption twice that of the image data size is assumed in this estimate. This estimate is based on using the focal pair method, so roughly 60% of the image data are used only in the initial stage of data processing and discarded in the final reconstruction. Only the individual selected particle images, not the original micrographs containing these particles, are included in this estimate.

[b]A 5-fold decrease in the image signal-to-noise ratio is assumed from 8 to 4 Å.

out data processing with available computing resources. The traditional mechanism of data management through a flat or tagged text file, or by using image headers, is error prone and difficult for data tracking and, thus, is inadequate for processing the substantially large data set needed for high-resolution studies. The scheme described above involves multiple computer programs. Each step requires the appropriate input of some user parameters and involves the proper selection of particle image files. The most repetitive procedure is the iterative refinement. Generally, it takes more than 10 iterative cycles to reach a 7- to 9-Å structure. In an effort to avoid any human handling errors of the data and to maximize the efficiency of using computing resources, the aforementioned programs have been incorporated into two software packages, which make the data management and data processing relatively easier and more convenient.

The first package is called IMIRS, which was originally coded for UNIX platforms with the refinement and reconstructions both parallelized to run on multiprocessor computer servers (Zhou *et al.*, 1998; Johnson *et al.*, 1997). This package has been ported to the widely available Microsoft Windows platforms and integrated with an SQL image database (http://hub.med.uth.tmc.edu/~hong/IMIRS) (Liang *et al.*, 2002). The client/server architecture of the IMIRS design divides the image processing task into a front-end component and a back-end or server component. An intuitive graphic user interface (GUI) provides novice users an easy access to the many data processing steps (as shown in Fig. 4) and constitutes the

front end. The database server constitutes the back end, with which many different front-end client applications communicate over the Internet. The database server maintains referential integrity, security, and logs, and ensures that operations can be painlessly recovered in the event of user mistakes and system failures. The data management tools provided in an SQL database are designed and optimized for applications that require not only large amounts of data, but also many simultaneous users across distributed computing environments. Thus, the use of relational image databases optimizes the tedious and error-prone data management tasks in 3-D reconstructions, allowing multiple users and many computers to work collaboratively and more independently, an inevitable situation encountered in projects targeting at atomic resolution.

The second package is called SAVR (http://ncmi.bcm.tmc.edu/~wjiang) (Jiang *et al.*, 2001a). This package has been designed to "glue" together the most CPU-intensive and iterative steps (or modules) in the IMIRS (Liang *et al.*, 2002) and the EMAN (Ludtke *et al.*, 1999) packages, using the scripting language Python. SAVR is portable across various UNIX-flavored platforms and has been parallelized to run on both shared and distributed memory platforms. SAVR also allows the incorporation of new algorithms and facilitates the management of the increasingly large data sets needed to achieve higher resolution reconstructions. More importantly, this package will allow users to perform checks on the results during various steps of the refinement to ensure the process is heading in the right direction. The package automatically e-mails the user with processing notification and data summaries at various stages. This software has been applied to solve two structures of icosahedral particles at subnanometer resolution (Jiang *et al.*, 2001a).

## V. Visualization and Structure Interpretation

### A. *Three-Dimensional Visualization Methods*

The 3-D visualization of electron densities of a virus structure is accomplished mostly with commercial volume and surface-rendering software packages with customized modules or programs. The most commonly used packages include Iris Explorer (NAG, Oxford, UK), which is available on both UNIX (SGI Irix and Linux) and Microsoft Windows platforms, and AVS (Advanced Visual Systems, Waltham, MA), which is available on the UNIX platform. Many enhancements have been added to both packages to accommodate specialized needs to visualize the large density volumes of virus structures, including import and export modules,

segmentation tools, as well as different ways of color coding the rendering (Spencer *et al.*, 1997; Sheehan *et al.*, 1996; Dougherty and Chiu, 1998, 2000).

Because surface rendering of large density volume data can be computationally prohibitive, it is necessary to dissect or segment individual structural components out of the entire virus reconstruction so that subnanometer-resolution features can be conveniently identified and compared (Zhou *et al.*, 2000, 2001) (Fig. 7; see Color Insert). Segmentation of individual components also allows nonicosahedral averaging of structurally similar components to enhance the $S/N$ ratio (He *et al.*, 2001). Only structural components within an icosahedral asymmetric unit are structurally unique and necessary for detailed examination. When desired, the entire viral particle can be generated by performing the 5-3-2 symmetry operations from the asymmetric unit (Fig. 7).

### *B. Visualization of Secondary Structure Elements*

A distinctive feature of 3-D maps at subnanometer resolution is the resolution of molecular internal structural features representative of secondary structure elements ($\alpha$ helices and $\beta$ sheets). The identification of these features, however, is not straightforward using surface representations alone and requires the combined use of different visualization techniques. Although it has been a common practice to display virus structures with shaded surface views, using a density cutoff or contour level equivalent to the molecular weight of the virus, such views do not readily reveal internal secondary structural features. At 7- to 9-Å resolution, long $\alpha$ helices appear as straight rods of densities ~5–6 Å in diameter when displayed at higher contour levels (e.g., above $2\sigma$), whereas large $\beta$ sheets appear as continuous surfaces at lower counter levels (Fig. 8). It should be cautioned, however, that small $\beta$ sheets containing two or three $\beta$ strands have a dimension similar to that of $\alpha$ helices and are difficult to distinguish at this resolution.

Therefore, a substantial portion of the secondary structure elements can be readily identified in 3-D maps calculated to 6- to 8-Å resolution by interactive visual inspection of the density volume, using 3-D volume-rendering techniques (Fig. 9; see Color Insert). Examination of the density range distribution can also be used as a means to verify secondary structure elements identified on the basis of shaded surface representations. For example, the gray density displays of density sections extracted from a 3-D volume are often useful to verify the assignment based on information such as the relative densities of the identified $\alpha$ helices and $\beta$

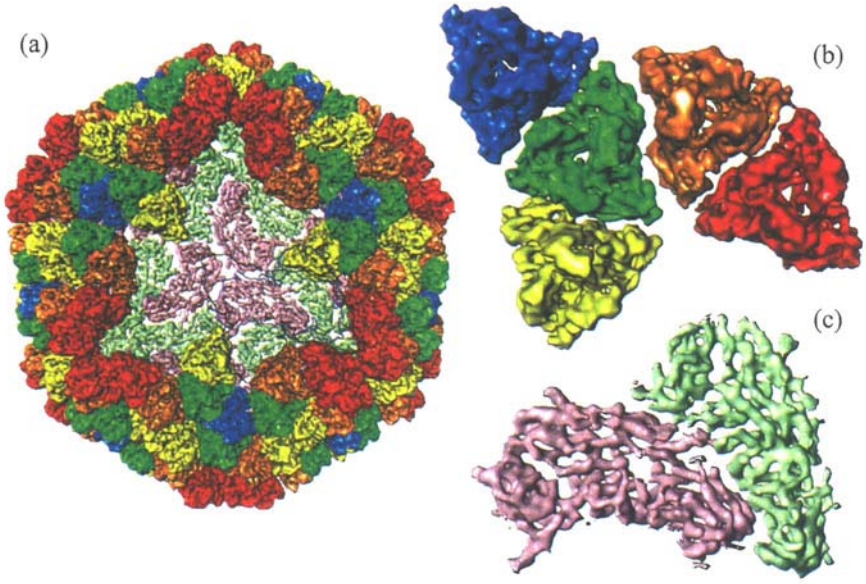


ZHOU AND CHIU, FIG. 7. Visualization of large virus particles via segmentation as illustrated by rice dwarf virus (RDV). (a) Full view of the entire RDV particle obtained by imposing icosahedral symmetry on an asymmetric unit segmented out from the original 3-D map. The subunits are segmented out and colored differently to facilitate visualization of intermolecular interactions. Each asymmetry unit (indicated by lines) contains four- and one-third trimers (in red, green, blue, yellow, and orange, respectively) of the outer shell protein P8 and two inner shell protein P3 monomers (in gray and aquamarine, respectively). In this display, 1 of the 20 triangular faces is removed to review the inner shell. (b and c) Close-up views of the unique subunits segmented out from the 3-D map, including the five P8 trimers on the outer shell (b) and the two P3 monomers on the inner shell (c) in each asymmetric unit.

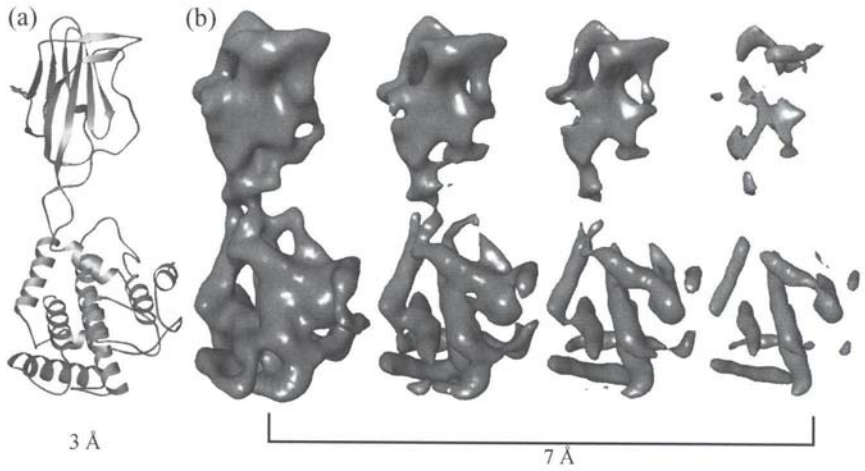


FIG. 8. Illustration of helices and $\beta$ sheets at 7 Å by a simulated density map. The atomic model of a VP7 monomer of bluetongue virus (Grimes *et al.*, 1998) was obtained from the Protein Data Bank and rendered as ribbons (a). The same model was then Gaussian filtered to 7 Å to generate a density map, which is displayed as shaded surfaces, from left to right, using gradually increasing contour levels (b). [Courtesy of Dr. Matthew L. Baker.]

sheets, and distances and twist angles between adjacent helices inside a helix bundle.

Interpretation of the membrane proteins in an envelope virus can be assisted by the identification of transmembrane $\alpha$ helices. Membrane proteins represent a special class of proteins because of the predominant presence of transmembrane helices connected by extramembrane loops and domains. For example, even at 10.5-Å resolution, a pair of transmembrane helices could be identified in the Semliki Forest virus E1 and E2 proteins (Fig. 10; see Color Insert).

Automatic pattern recognition tools such as *helixHunter* have been developed to perform the tedious manual identification of helices longer than 2.5 turns (Jiang *et al.*, 2001b). *helixHunter* uses a cylinder of 5 Å in diameter as a generic helix template and carries out an exhaustive 3-D cross-correlation search in a 3-D density map to identify the locations of helices. This objective and automatic approach involves a multistep process of cross-correlation, density segmentation, quantification, and helix identification as well as an explicit description of the helices. For visualization purposes, final helices can be annotated as cylinders (such as those modeled in Figs. 9 and 10), which can be described by six parameters (three for center, two for orientation, and one for length).

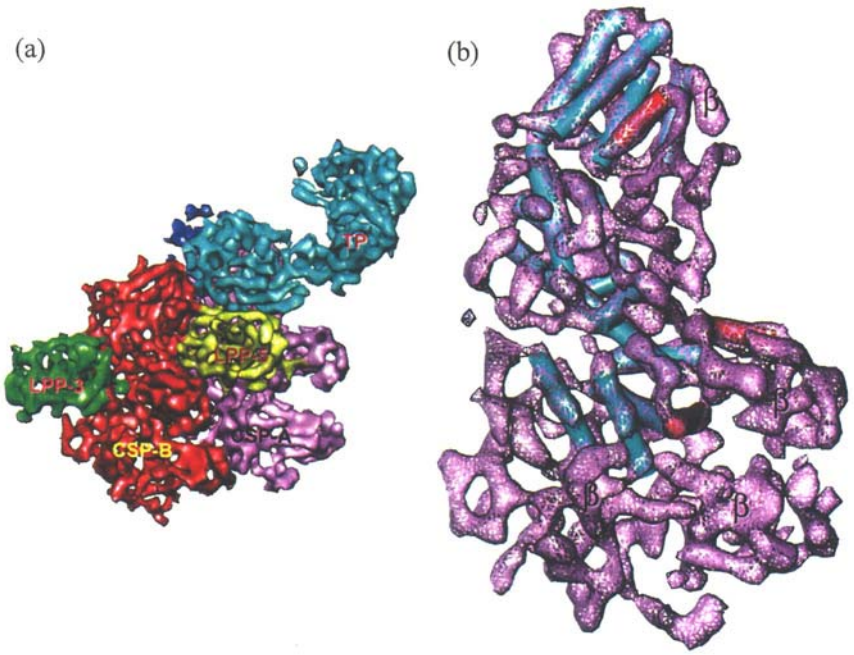


ZHOU AND CHIU, FIG. 9. Visualization of secondary structures in cytoplasmic polyhedrosis virus (CPV) capsid shell protein (Liang *et al.*, 2002; Zhou *et al.*, 2003). (a) An asymmetric unit extracted from the 8-Å structure of CPV. The structural components within the asymmetric unit are labeled, including one turret protein (TP, in light blue), two capsid shell protein (CSP) molecules (CSP-A, in red, and CSP-B, in gray), and two large protrusion protein molecules (the 5-fold proximal LPP-5 in yellow and 3-fold proximal LPP-3 in green). (b) CSP-A displayed at a higher density contour level, using wire frame representation, superimposed with visually identified helices, which were modeled as 5-Å-diameter cylinders. A total of 18 helices were identified in CSP-A, 14 (aquamarine) of which are structurally homologous to those in bluetongue virus VP3 and 4 (red) of which are unique to CPV. Several $\beta$ sheet-rich regions were also identified and are indicated ($\beta$).

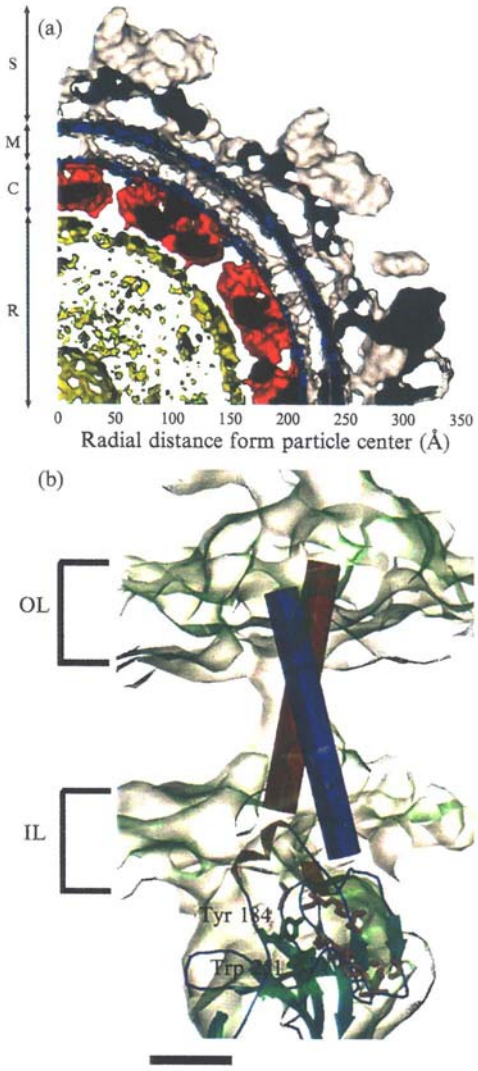


ZHOU AND CHIU, FIG. 10. Identification of transmembrane helices in Semliki Forest virus (SFV) E1 and E2 (Mancini *et al.*, 2000). (a) Shaded surface view of a central slab reveals the multiple shell organization of SFV. SFV is an envelope virus consisting of an RNA core (R) (yellow), a nucleocapsid made of 240 copies of protein C (C), which is enclosed by a lipid bilayer membrane (M) (inner and outer leaflets shown in blue) decorated with 80 glycoprotein spikes (S) (shown in white). (b) Transmembrane regions of the E1 and E2 densities interacting with the capsid are shown. The C protein is shown as a ribbon diagram. The positions of the inner leaflet (IL; radius, 213 Å) and the outer leaflet (OL; radius, 261 Å) of the membrane are marked. The putative $\alpha$-helical transmembrane segments for E1 and E2 are depicted with a paired helical segment from a known protein structure, demonstrating that the dimensions and the topology of the density are consistent with a pair of helices. The transmembrane domains are seen as paired rods of density approximately 10 Å wide, separated at the top by approximately 10 Å and twisting about each other. Scale bar: 15 Å. Adapted from Mancini *et al.* (2000) with permission from the publisher and the authors.

### C. *Derivation of Folds*

The fold of a protein can be described by its overall topology, which includes the spatial arrangement and the connectivity of the secondary structure elements of the polypeptide chain into the tertiary structure (Lo Conte *et al.*, 2000; Orengo *et al.*, 1997). In a large protein, a single chain may form one or several distinct domains, each with a particular fold. However, $\alpha$ helices and $\beta$ sheets identified either manually or automatically do not contain any information for mapping the identified secondary structure elements to their amino sequences in the resolution regimen from 7–9 Å. When the fold is relatively simple, it is possible to assign such information by correlating existing biochemical and structural information. The map of the hepatitis B virus core protein has a simple fold with a pair of bundled helices and represents the first time that the fold of a protein has been derived by image analysis of single particles (Böttcher *et al.*, 1997a) (Fig. 11; see Color Insert). The putative amino and carboxyl termini were identified by integrating its known biochemical and immunological information. In this particular case, undecagold-labeled cysteine was engineered onto its C terminus (Zlotnich *et al.*, 1997). In addition, difference imaging was used to locate a peptide of 10 amino acids inserted onto the N terminus of the core protein (Conway *et al.*, 1998). The availability of a large body of biochemical mutagenesis data together with chemical labeling studies made it possible to establish a fold model of the core protein (Fig. 12; see Color Insert) (Böttcher *et al.*, 1997a; Conway *et al.*, 1998). The predicted fold is in good agreement with that subsequently determined by X-ray crystallography at 3.3 Å (Wynne *et al.*, 1999).

For more complex structures, it is possible to combine electron cryomicroscopy structures with sequence-based secondary structure predictions to interpret the observed secondary structure elements. In the outer shell protein P8 of rice dwarf virus (RDV), where nine helices were predicted in the domain formed by the N and C termini, it was possible to match the lengths of the helices identified in the 3-D density map to those predicted from a consensus secondary structure analyses (Fig. 13a; see Color Insert). The connections between the helical densities can be seen in the lower domain of P8, allowing us to establish a rough backbone model for the lower domain of P8 (Zhou *et al.*, 2001).

To assess the accuracy of such a prediction, *DejaVu* (Kleywegt and Jones, 1997) and *COSEC* (Mizuguchi and Lio, 1995) can be used to perform spatial fold recognition. A successful match in the helix arrangement between the *helixHunter* results of a structure in the Protein Data Bank

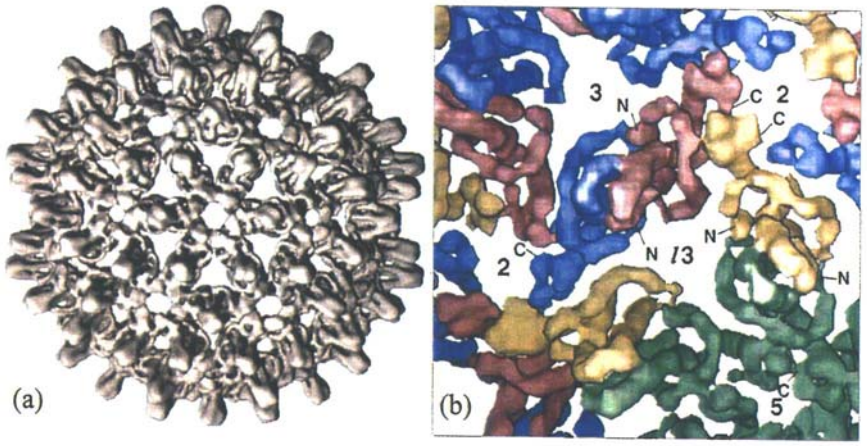


ZHOU AND CHIU, FIG. 11. Identification of the path of each polypeptide of the hepatitis B virus core protein (Böttcher *et al.*, 1997a). (a) Shaded surface representation of the T=4 HBV core structure determined at 7.4-Å resolution, viewed down a strict 2-fold axis. (b) Close-up view down a local 3-fold axis (*l*3). The positions of neighboring strict 2-fold, 3-fold, and 5-fold axes are marked. The density has been colored to indicate the four symmetrically independent monomers. The path of each polypeptide is revealed by using a higher density threshold for the display. The positions of the putative N and C termini of the polypeptide are indicated. [Adapted from Böttcher *et al.* (1997b) with permission from the author and the publisher.]

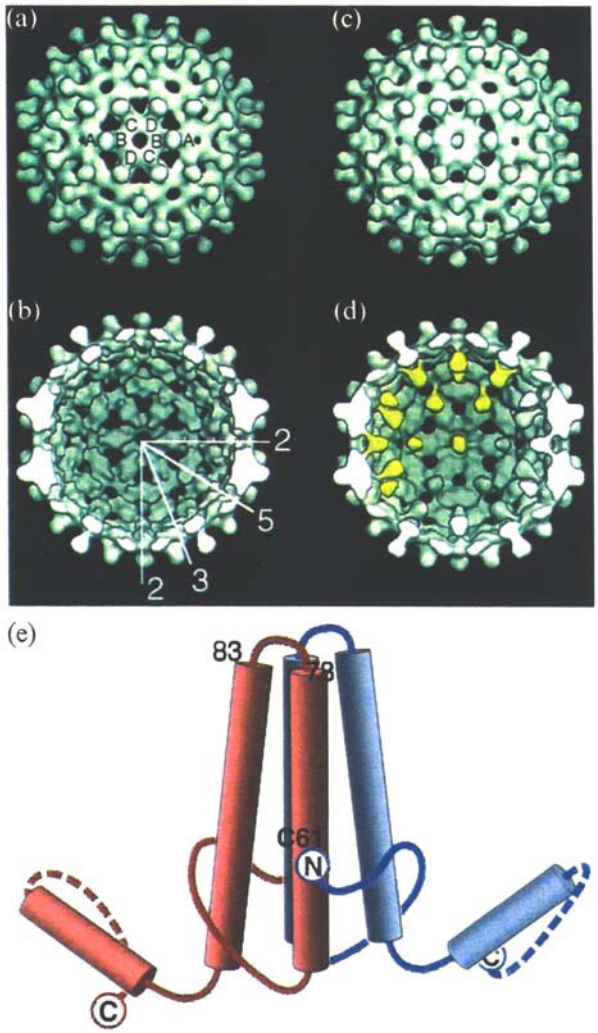


ZHOU AND CHIU, FIG. 12. Identification of specific amino acid residuals by difference imaging with chemical labels. (a and b) Three-dimensional structure of empty HBV Cp147 capsid at 17 Å. (c and d) Three-dimensional structure (20 Å) of the HBV $Cp^{*}$ 150 capsid with its C terminus labeled with undecagold label $Au_{11}$. (e) Model of the HBV capsid protein dimer with locations of the amino acids localized by difference imaging, including the C terminus by gold labeling, the N terminus by an octapeptide insertion (Conway *et al.*, 1998), and the loop covering residues 78–93. [Adapted from Zlotnick *et al.* (1997) and Conway *et al.* (1998) with permission from the publishers.]

suggested a possible fold homolog. Six of the nine helices within the lower domain of RDV P8 subunit were matched to bluetongue virus VP7 (centroid RMS <5 Å) even though these proteins have only remote or no sequence similarity (<20%).

In addition, an individual protein or portions of a protein within a macromolecular complex may have a homologous structure. Once a homologous fold has been identified, it is necessary to place this structure back into the entire complex. *foldHunter*, a template-based cross-correlation tool, automatically searches all possible rotations and translations for the best fit of the homologous structure to the density map of the macromolecule (Jiang *et al.*, 2001b). In RDV P8, it was possible to identify the middle sequence segment to be structurally similar to the $\beta$-sheet domain of VP7 of the bluetongue virus. Figure 13b shows the localization of the putative jelly-roll $\beta$-sandwich fold of bluetongue virus in the density in the upper domain of RDV P8. By combining this fold identification result with the earlier *helixHunter* results, a model for the entire structure of P8 can be derived (Fig. 13b).

### *D. Toward Near-Atomic Resolution: Three-Dimensional modeling*

Electron cryomicroscopy has been used to determine near-atomic resolution structures of two-dimensional crystals (Henderson *et al.*, 1990; Nogales *et al.*, 1998) and, therefore, in principle, may possibly be used to reach the same resolution in determining the structures of icosahedral virus particles. Modern electron cryomicroscopes are capable of recording images containing data at this resolution. A trivial limiting factor currently facing us is the digitization of data. The availability of a high-throughput scanner or of a high-resolution CCD camera will be helpful in this regard to generate image data in a digital form within a reasonable amount of time. A nontrivial limitation seems to lie in the development of a more powerful image-processing algorithm for improved accuracy in the refinement of orientation and center parameters and in the determination of CTF, particularly in those micrographs with residual astigmatisms. Finally, for larger particles, the correction for curvature of the Ewald sphere due to the depth of field limitation must be taken into account (DeRosier, 2000; Jensen, 2001). In any case, tens of thousands of particle images will need to be processed (Saad *et al.*, 2001). Thus, a powerful, efficient, user-friendly, and data management-capable software package is certainly required to accomplish the massive task of data processing for near-atomic resolution reconstructions.

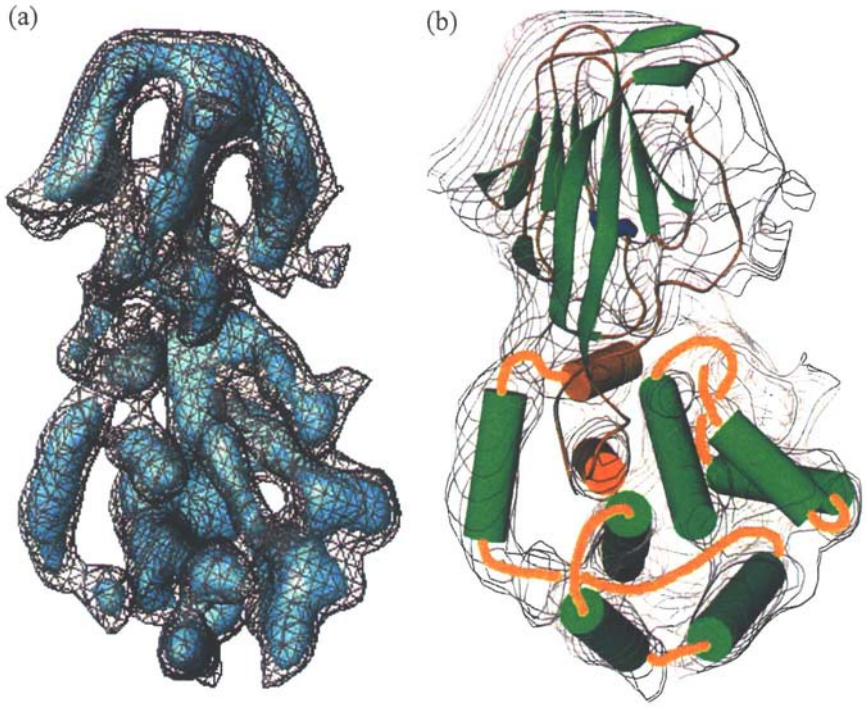


ZHOU AND CHIU, FIG. 13. Interpretation of subnanometer-resolution structure through integration of bioinformatics and secondary structure assignment (Zhou *et al.*, 2001). (a) A side view of the density map of a P8 monomer extracted from the 6.8-Å RDV structure. The higher density features are shown as shaded surfaces and their connectivities are revealed in the wire frame representation shown at a relatively lower density contour level. (b) Interpreted folds of the secondary structure elements in RDV P8. Each P8 contains a lower domain with nine helices and an upper $\beta$-barrel domain. The homologous bluetongue virus VP7 $\beta$-barrel fold was identified by *foldHunter* and shown as ribbon. [Picture courtesy of Dr. Matthew L. Baker.]

## VI. Conclusion

Structural determination of icosahedral viruses at subnanometer resolution by electron cryomicroscopy has become routine about 15 years after the first cryomicroscope virus structure at about 40 Å was reported. With the current approach of combining these structures and other bioinformatics analyses, it is possible to derive a pseudo-atomic model of an entire virion in some favorable cases. This capability has transformed electron cryomicroscopy to a method of choice for rapidly solving the structures of viruses and their complexes with other factors. By combining the electron cryomicroscopy structures of a virus with the X-ray crystal structures of its components, it is possible to describe structure changes during viral assembly and define the interactions between the virus and its cellular factors. Most important, the prospect is indeed promising for obtaining 3-D reconstructions of viruses approaching atomic resolution by using electron cryomicroscopy alone. While virologists enjoy the imaging power that electron cryomicroscopy offers for understanding the structure–function relationships of viral assembly and infection, the advancement of this technique toward near-atomic resolution will also benefit other efforts to improve the resolution of structural determination of macromolecular complexes with less or no symmetry.


## Acknowledgments

The research activities described here have been supported in part by grants from the NIH (P41RR02250, AI43656, and AI38469 to W.C., AI46420 and CA94809 to Z.H.Z.), the Welch Foundation (Q1242 to W.C. and AU-1492 to Z.H.Z.), the March of Dimes Birth Defects Foundation (5-FY99-852 to Z.H.Z.), and the American Heart Association (0240216N to Z.H.Z.), Z.H.Z. is a Pew Scholar in Biomedical Sciences. We thank Dr. Michael Schmid, Dr. Wen Jiang, Jacob Zachariah, and Sanket Shah for their comments on this manuscript.


## References


Baker, T. S., and Cheng, R. H. (1996). *J. Struct. Biol.* **116,** 120–130.

Baker, T. S., Drak, J., and Bina, M. (1988). *Proc. Natl. Acad. Sci. USA* **85,** 422–426.

Baker, T. S., Olson, N. H., and Fuller, S. D. (1999). *Microbiol. Mol. Biol. Rev.* **63,** 862–922.

Böttcher, B., and Crowther, R. A. (1996). *Structure* **4,** 387–394.

Böttcher, B., Wynne, S. A., and Crowther, R. A. (1997a). *Nature* **386,** 88–91.

Böttcher, B., Wynne, S. A., and Crowther, R. A. (1997b). *Hitachi Instr. News Electron Microsc. Ed.* **32,** 3–8.

Chiu, W. (1978). *Scanning Electron Microsc.* **1,** 569–580.

Chiu, W., Knapek, E., Jeng, T. W., and Dietrick, I. (1981). *Ultramicroscopy* **6,** 291–296.

Conway, J. F., and Steven, A. C. (1999). *J. Struct. Biol.* **128,** 106–118.

Conway, J. F., Cheng, N., Zlotnick, A., Wingfield, P. T., Stahl, S. J., and Steven, A. C. (1997). *Nature* **386,** 91–94.

Conway, J. F., Cheng, N., Zlotnick, A., Stahl, S. J., Wingfield, P. T., and Steven, A. C. (1998). *Proc. Natl. Acad. Sci. USA* **95,** 14622–14627.

Crowther, R. A. (1971). *Philos. Trans. R. Soc. Lond. B Biol. Sci.* **261,** 221–230.

Crowther, R. A., Amos, L. A., Finch, J. T., DeRosier, D. J., and Klug, A. (1970a). *Nature* **226,** 421–425.

Crowther, R. A., DeRosier, D. J., and Klug, A. (1970b). *Proc. R. Soc. Lond. B Biol. Sci.* **317,** 319–340.

DeRosier, D. J. (2000). *Ultramicroscopy* **81,** 83–98.

Dougherty, M., and Chiu, W. (2000). *Microsc. Microanal.* **6,** 282–283.

Dougherty, M. T., and Chiu, W. (1998). *In* "Microscopy and Microanalysis 1998" (G. W. Bailey, K. B. Alexander, W. G. Jerome, M. G. Bond, and J. J. McCarthy, Eds.), pp. 452–453. Springer-Verlag, Atlanta, GA.

Erickson, H. P., and Klug, A. (1970). *Philos. Trans. R. Soc. Lond. B. Biol. Sci.* **261,** 105–118.

Frank, J. (1979). *J. Microsc.* **117,** 25–38.

Fuller, S. D. (1987). *Cell* **48,** 923–934.

Fuller, S. D., Butcher, S. J., Cheng, R. H., and Baker, T. S. (1996). *J. Struct. Biol.* **116,** 48–55.

Grimes, J. M., Burroughs, J. N., Gouet, P., Diprose, J. M., Malby, R *et al.* (1998). *Nature* **395,** 470–478.

He, J., Schmid, M. F., Zhou, Z. H., Rixon, F., and Chiu, W. (2001). *J. Mol. Biol.* **309,** 903–914.

Henderson, R., Baldwin, J. M., Ceska, T. A., Zemlin, F., Beckmann, E., and Downing, K. H. (1990). *J. Mol. Biol.* **213,** 899–929.

Jensen, G. J. (2001). *J. Struct. Biol.* **133,** 143–155.

Jiang, W., and Chiu, W. (2001). *Microsc. Microanal.* **7,** 329–334.

Jiang, W., Li, Z., Zhang, Z., Booth, C. R., Baker, M. L., and Chiu, W. (2001a). *J. Struct. Biol.* **136,** 214–225.

Jiang, W., Baker, M. L., Ludtke, S. J., and Chiu, W. (2001b). *J. Mol. Biol.* **308,** 1033–1044.

Jiang, W., Li, Z., Zhang, Z., Baker, M. L., Prevelige, P. E., and Chiu, W. (2003). *Nat. struct. Biol.* **10,** 131–135.

Johnson, O., Govindan, V., Park, Y., and Zhou, Z. H. (1997). *In* "Proceedings of the 4th International Conference in High Performance Computing," pp. 517–521. IEEE Computer Society Press, Los Alamitos, California.

Kleywegt, G. J., and Jones, T. A. (1997). "Detecting Folding Motifs and Similarities in Protein Structures," pp. 525–545. Academic Press, London.

Liang, Y., Ke, E. Y., and Zhou, Z. H. (2002). *J. Struct. Biol.* **137,** 292–304.

Lo Conte, L., Ailey, B., Hubbard, T. J., Brenner, S. E., Murzin, A. G., and Chothia, C. (2000). *Nucleic Acids Res.* **28,** 257–259.

Ludtke, S. J., Baldwin, P. R., and Chiu, W. (1999). *J. Struct. Biol.* **128,** 82–97.

Ludtke, S. J., Jakana, J., Song, J.- L., Chuang, D., and Chiu, W. (2001). *J. Mol. Biol.* **314,** 253–262.

Mancini, E. J., Clarke, M., Gowen, B. E., Rutten, T., and Fuller, S. D. (2000). *Mol. Cell* **5,** 255–266.

Mizuguchi, K., and Go, N. (1995). *Protein Eng.* **8,** 353–362.

Nogales, E., Wolf, S. G., and Downing, K. H. (1998). *Nature* **391,** 199–203.

Orengo, C. A., Michie, A. D., Jones, S., Jones, D. T., Swindells, M. B., and Thornton, J. M. (1997). *Structure* **5,** 1093–1108.

Prasad, B. V.V., Wang, G. J., Clerx, J. P.M., and Chiu, W. (1988). *J. Mol. Biol.* **199,** 269–275.

Saad, A., Ludtke, S. J., Jakana, J., Rixon, F. J., Tsuruta, H., and Chiu, W. (2001). *J. Struct. Biol.* **133,** 32–42.

Schmid, M. F., Jakana, J., Matsudaira, P., and Chiu, W. (1993). *J. Mol. Biol.* **230,** 384–386.

Sheehan, B., Fuller, S. D., Pique, M. E., and Yeager, M. (1996). *J. Struct. Biol.* **116,** 99–106.

Spencer, S., Sgro, J., Dryden, K., Baker, T., and Nibert, M. (1997). *J. Struct. Biol.* **120,** 11–21.

Thon, F. (1971). *In* "Electron Microscopy in Material Sciences," pp. 572–625. Academic Press, New York.

Thuman-Commike, P. A., and Chiu, W. (2000). *Micron* **31,** 687–711.

Trus, B. L., Roden, R. B., Greenstone, H. L., Vrhel, M., Schiller, J., and Booy, F. P. (1997). *Nat. Struct. Biol.* **4,** 411–418.

van Heel, M. (1987). *Ultramicroscopy* **21,** 95–100.

van Heel, M., Gowen, B., Matadeen, R., Orlova, E. V., Finn, R *et al.* (2000). *O. Rev. Biophys.* **33,** 307–369.

Wynne, S. A., Crowther, R. A., and Leslie, A. G. (1999). *Mol. Cell* **3,** 771–780.

Zhou, Z. H., and Chiu, W. (1993). *Ultramicroscopy* **49,** 407–416.

Zhou, Z. H., Prasad, B. V., Jakana, J., Rixon, F. J., and Chiu, W. (1994). *J. Mol. Biol.* **242,** 456–469.

Zhou, Z. H., He, J., Jakana, J., Tatman, J. D., Rixon, F. J., and Chiu, W. (1995). *Nat. Struct. Biol.* **2,** 1026–1030.

Zhou, Z. H., Hardt, S., Wang, B., Sherman, M. B., Jakana, J., and Chiu, W. (1996). *J. Struct. Biol.* **116,** 216–222.

Zhou, Z. H., Chiu, W., Haskell, K., Spears, H.Jr., Jakana, J *et al.* (1998). *Biophys. J.* **74,** 576–588.

Zhou, Z. H., Chen, D. H., Jakana, J., Rixon, F. J., and Chiu, W. (1999). *J. Virol.* **73,** 3210–3218.

Zhou, Z. H., Dougherty, M., Jakana, J., He, J., Rixon, F. J., and Chiu, W. (2000). *Science* **288,** 877–880.

Zhou, Z. H., Baker, M. L., Jiang, W., Dougherty, M., Jakana, J *et al.* (2001). *Nat. Struct. Biol.* **8,** 868–873.

Zhou, Z. H., Zhang, H., Jakana, J., Lu, X.-Y., and Zhang, J.-Q. (2003). *Structure* **11,** in press.

Zlotnick, A., Cheng, N., Stahl, S. J., Conway, J. F., Steven, A. C., and Wingfield, P. T. (1997). *Proc. Natl. Acad. Sci. USA* **94,** 9556–9561.